Digital Twins and CFD simulations for accurate sensor positioning

Oscar Roman[1,2], Maarten Bassier[3], Silvia Ricciuti[4], Elisa Mariarosaria Farella[2], Fabio Remondino[2], Diego Viesi[4]

[1] Department Information Engineering and Computer Science (IECS), University of Trento, Trento, Italy - oscar.roman@unitn.it

[2] 3D Optical Metrology (3DOM) unit, Bruno Kessler Foundation (FBK), Trento, Italy web: http://3dom.fbk.eu
oroman@fbk.eu, elifarella@fbk.eu, remondino@fbk.eu

[3] Dept. of Civil Engineering, TC Construction - Geomatics, KU Leuven - Faculty of Engineering Technology, Ghent, Belgium
maarten.bassier@kuleuven.be

[4] Center for Sustainable Energy, Bruno Kessler Foundation (FBK), Trento, Italy - sricciuti@fbk.eu, viesi@fbk.eu

Keywords: Automation in constructions, BIM, Computational Fluid Dynamics, Deep Learning, Digital Twin, Energy efficiency

Abstract
Building renovation to improve energy efficiency is crucial for reducing CO_2 emissions, aligning with the goal of achieving net-zero emissions by 2050. This task requires a holistic approach that encompasses retrofitting outdated systems, enhancing thermal insulation, and integrating renewable energy sources. Simulating different indoor environmental conditions and technological systems within Digital Twin (DT) before interventions is crucial for optimizing energy efficiency. Simulations can support the proper installation of heating and cooling devices and facilitate the deployment of advanced technologies, including smart Heating, Ventilation, and Air Conditioning (HVAC) systems, energy-efficient lighting, and automated energy management solutions. The use of Artificial Intelligence (AI) in simulations allows for the precise sizing of HVAC systems, including heat pumps and related devices, by accurately modelling demand profiles and optimizing sensor placement based on the geometries of DTs.
This study, conducted as part of the Horizon Europe InCUBE project[1], explores a real-world use-case at the Centro Servizi Culturali Santa Chiara in Trento, Italy. It introduces an innovative approach that integrates 3D surveying, computational fluid dynamics (CFD), and digital twin (DT) geometries to enhance the analysis of indoor heat distribution. The proposed data-driven pipeline optimizes sensor placement within indoor spaces, ensuring precise system design, improving performance and energy efficiency, and minimizing energy waste while preventing the oversizing of technological systems.

1. Introduction

Digital Twins are revolutionizing the landscape of civil engineering (Hu et al., 2023), manufacturing (Liu et al., 2024a), energy sector (Arowoiya et al., 2024) and maintenance processes (Gosavi et al., 2024). For the built environment, and in particular for buildings, a digital replica serves as a powerful tool for both simulating various scenarios and monitoring real-time conditions. These replicas typically consist of two key components: (i) a geometric digital twin (gDT), which represents the building's physical structure and spatial characteristics (Pan et al., 2024), and (ii) a dynamic interface linked to real-time data (Liu et al., 2024b), enabling continuous monitoring and actionable insights. At the same time, graph-based structures (Bassier et al., 2024), with nodes organized into hierarchical frameworks, are increasingly important for integrating information from diverse domains. These structures efficiently integrate geometric data with domain-specific information, offering advantages in data storage, ease of updating and flexibility in filtering or querying information.
An efficient and holistic Scan-to-BIM (Building Information modelling) method for generating DTs tailored to energy applications and optimizing Building Energy Management Systems (BEMS) remains largely absent.

1.1 Paper objectives

The proposed workflow enhances sensor placement by leveraging Computational Fluid Dynamics (CFD) simulations to analyze indoor heat diffusion and identify thermal stagnation zones, where temperature remains stable with minimal fluctuations. This facilitates the resizing of HVAC systems, reducing their overall size while ensuring precise climate control and enhancing energy efficiency assessments. By simulating heat flow across various scenarios, the approach determines optimal sensor placement, ensuring accurate system setpoints, improving comfort, and maximizing energy savings. The pipeline comprises two main parts: (i) geometric reconstruction and (ii) energy-related simulation for optimal sensor positioning. The first part involves:

- Reconstruction of building's structural elements (gDT) using a Deep Learning (DL) method (Roman et al., 2024b).
- Development of a graph-based framework integrating geometric and energy data nodes for creating a comprehensive dataset (Bassier et al., 2024).
- Definition of a Topologic BIM (TBIM) model as a node-based framework within the main graph architecture.

The second part focuses on the following objectives:

- Computational Fluid Dynamics (CFD) simulations to assess indoor heat diffusion and environmental dynamics.
- Heat distribution analysis to identify stable temperature zones across scenarios.

The final step refines sensor placement by targeting thermally stable zones with minimal heat fluctuations through simulation image analysis. This enhances data accuracy, optimizes system performance, and boosts energy efficiency.

2. Related works

DTs combine geometric elements with real-time and informative data. While the geometric model and some semantic details can be extracted from surveyed data, additional information often requires manual integration due to the diverse data needed for structural, management, and energy efficiency analyses. Graph-based structures are becoming increasingly important for bridging the gap between these components. Several studies (Aish et al., 2018; Jabi et al., 2021) have explored the integration of these data structures with the BIM environment, leveraging the

[1] https://incubeproject.eu/

hierarchical relationships between entities commonly found in IFC files.
In the field of energy efficiency, applications have focused on linking European regulations[2] through Information Loading Dictionaries (ILDs), with various methodologies being defined and practically applied (Olasolo-Alonso et al., 2023).
Recent studies integrate Virtual Reality (VR) with BIM to visualize energy analysis and Technical Building Equipment (TBE) (Blut et al., 2024). An energy building graph structure has been proposed by (Yang et al., 2024), extended to the urban scale (Ma et al., 2024), but the connection between building geometry and energy systems, devices, and components remains incomplete and requires further integration.
Some interesting applications (Ramón-Constantí et al., 2024) focus on matching thermal images with point clouds to conduct energy analyses and assess the results. A method for thermal texture mapping ensuring geometric and radiometric consistency by registering thermal images to 3D point clouds for accurate temperature measurements has been proposed by (Lin et al., 2019). Meanwhile, applications utilizing DL networks for physics-informed simulations are being increasingly applied (Wandel et al., 2020).

3. General methodology

The presented workflow (Figure 1) outlines a data-driven approach for optimizing sensor placement in indoor environments. As discussed in Section 1.1, the process systematically integrates geometric data (steps 1A to 2B) and metadata (point 2C, 2D) with energy analysis and CFD simulations (steps 3 to 5) to refine sensor positioning (step 6).

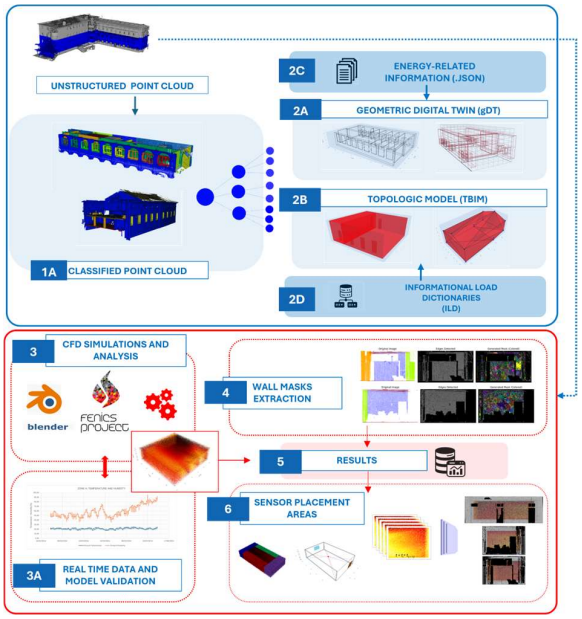

Figure 1. Scheme of the proposed workflow.

The complete workflow, starting from the classified point cloud (step 1A) consists of:

- Geometric Digital Twin creation (2A): the geometric Digital Twin (gDT) model is derived from classified point cloud data (Section 3.2). It represents a geometric structure of both primary and secondary building elements.
- Topologic BIM (TBIM) model (2B): TBIM is developed to store previously computed geometry, volumetric and spatial information (Section 3.3). The TBIM is a volumetric model ready to be enriched with metadata and ILDs.
- Metadata collection (2C, 2D): energy-related metadata, device characteristics, volumetric data, and building usage patterns are collected and stored in the primary graph database to facilitate enhanced analyses and data-driven insights (Section 3.4).
- Energy model and simulation (3): thermal analysis and CDF simulations are performed using FEniCS platform (Logg et al., 2011) to predict temperature distributions and identify key areas of heat variation (Sections 3.4 and 3.5).
- Model calibration (3A): previous analyses are calibrated based on the data coming from Internet of Things (IoT) devices.
- Wall masks extraction (4): from the classified point cloud, ortho images of the walls are generated and masks are created to identify available positions for device placement (Section 3.6). These wall masks are then matched with heat distribution data from simulations to exclude unsuitable areas, such as openings and clutter, ensuring optimal sensor positioning.
- Sensor placement optimization (5, 6): from results of simulations and masks, temperature sensors are strategically placed key zones with stable thermal conditions to optimize monitoring and enhance energy efficiency (Section 3.7).

3.1 Dataset used

The study utilizes the Santa Chiara building dataset (Trento, Italy), gathered for the InCUBE project, focusing on a selected group of first-floor offices in the central wing (Figure 2). Point cloud data and panoramic images are accessible via the GitHub repository[3] (Roman et al., 2023).
The analyzed area primarily consists of office spaces, oriented approximately along the North-South axis.
For ex-ante monitoring, several IoT devices from the InCUBE project partner Tera Srl were installed on the first floor. These include BEETA Box IoT edge computing gateways, eleven Z-Wave multiparameter sensors (measuring temperature and humidity), thirty-five smart switches, and a CO_2 sensor.

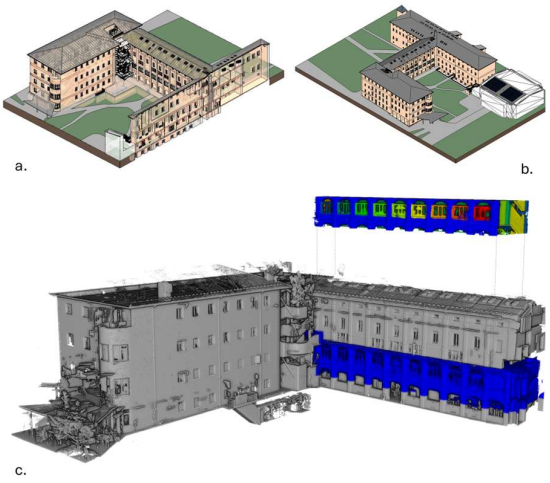

Figure 2. View of the Santa Chiara buildings (a and b). The first floor of the central wing used in the experiments (c).

The area of interest (Figure 3), denominated *Zone A*, consists of two distinct rooms. Geometric details about the indoor spaces are shown in Table 2.
The devices have provided valuable data, which has been instrumental in calibrating the analysis of heat transfer. The

[2] https://eur-lex.europa.eu/eli/dir/2018/844/oj

[3] https://github.com/3DOM-FBK/InCUBE

rooms have been divided into two main areas, with one or more sensors installed in each, as shown in Figure 3.
In particular, *sensor_01* was installed in the *Zone A1*, while *sensor 02* in the *Zone A2*. For all analyses in this study, the reported results for *Zone_A* represent the mean values averaged across the two rooms, as stored and transmitted by the IoT device.
Multiple sensors collect data on temperature (Figure 4), humidity (Figure 5), and CO_2 levels.
The data, recorded at one-minute intervals from February 27 to June 6, 2024, allows for both monthly and daily analyses.

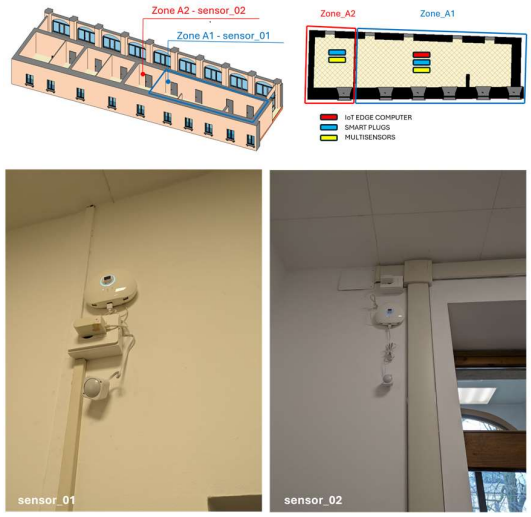

Figure 3. The placement of sensors in *Zone A1* and *Zone A2* (top). Temperature and humidity sensors installed (below).

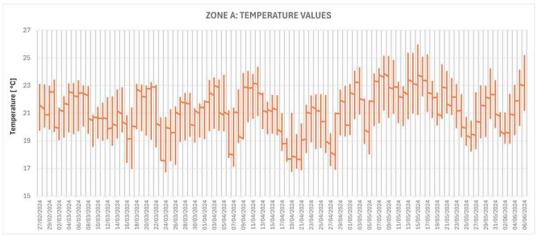

Figure 4. Temperature values in *Zone A*.

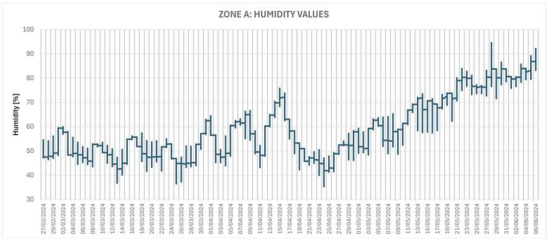

Figure 5. Humidity values in *Zone A*.

3.2 Geometric Digital Twin (gDT)

Following the workflow outlined in (Roman et al., 2024b), the point cloud was classified using Point Transformer version 3 (Wu et al., 2024), while Pointcept (Zhao et al., 2021) was utilized for instance segmentation. For window detection, GroundingDINO (Liu et al., 2023) was leveraged, achieving a mean Intersection over Union (mIoU) of 0.58. It is important to note that the dataset does not include any RGB data, limiting the detection process.

Based on the workflow presented in (Roman et al., 2024a; Roman et al., 2024b), structural building elements are reconstructed from the point cloud data. The focus is on primary components such as walls, floors, and ceilings, as well as secondary elements like windows and doors.
The enhanced graph not only maps structural elements but also provides detailed geometric metadata associated with these components. The class and object_id store geometric information and spatial definitions, along with classified points associated with each object_id. Structural elements and their metadata are finally stored in a JSON-based RDF graph file (Bassier et al., 2024), which organizes key information such as geometric properties, object_ids, locations, and orientations.

3.3 Topologic BIM model (TBIM)

The proposed workflow enhances the traditional graph data structure related to the gDT by incorporating a Topologic Building Information Model (TBIM) (Jabi et al., 2021), which integrates geometric data with volumetric information, building location, room usage (aligned with European standards).
As noted earlier, the topological map (Roman et al., 2024a) serves as the foundation for the generation of 2D indoor spaces, computed at various z-levels. The edges defined by the map are then used as information for the TBIM, which considers vertices and edges of walls, floors, and ceilings reconstructed in the gDT (Section 3.2) as inputs to define the 3D volume (Figure 6).
The key steps in the workflow are: (i) extracting building elements from the gDT to create the topological map, (ii) defining the main indoor space volumes, (iii) generating the meshes for the analyses, and (iv) linking metadata to the computed volumes. This approach generates an additional node in the graph, based on Load Dictionaries (ILDs), to assign metadata relevant for simulations and analyses, including orientations and volumes.
The final output is a comprehensive node-structured graph that integrates both geometric and spatial data with energy-related metadata, represented using a vocabulary-based information model.

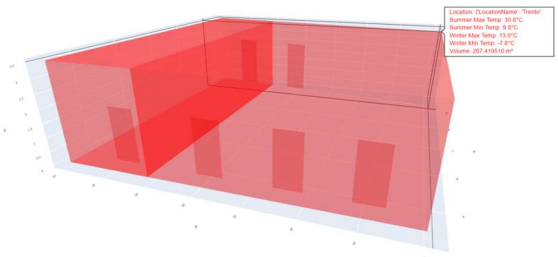

Figure 6. The TBIM model where metadata are stored.

3.4 Model and boundary conditions for simulations

Analyzing sensor placement in thermally stable zones with minimal temperature fluctuations ensures accurate data collection, enabling precise climate control, enhancing system design, preventing oversizing, and improving energy efficiency without compromising performance.

3.4.1 Model for simulation

The workflow generates .obj meshes of building volumes (Section 3.3), which define the surface model for energy simulations. These meshes generated with a semi-automatic process have irregular shapes that differ from manually produced meshes.
As a result, they are not fully compatible with OpenFOAM (OpenCFD Ltd) software, which is specifically designed for CFD

applications. To address this challenge, we decided to leverage the FEniCS (Logg et al., 2011) library for simulations, adapting it to suit our CFD needs (Section 3.5).
The primary operation involves converting the geometric model generated through the geometric Digital Twin workflow to make it compatible with the FEniCS library.
By using the *refine(mesh)* command, the mesh density can be increased, allowing for deeper insights in the analysis.
In this process, U-values (thermal transmittance) derived from ILDs are assigned to each mesh according to its classification. U-values are assigned to each building element based on the Energy Performance of Buildings Directive (EPBD) and may slightly differ from those reported in (Ziozas et al., 2024) due to specific material property assumptions.
Additionally, heating system data follow the guidelines of (Maduta et al. 2023) (Table 1) and comply with European regulations.
This approach allows us to determine the U-value, area, position, orientation, dimensions, and class type of each element with precision. Heat sources, in this case, radiators, have been punctually inserted in the model in the real position.

Element	U computation	U-value W/m^2K
External walls	$U_W = \left(\sum_{i=1}^{n} \frac{1}{\lambda_{i,W} \cdot d_{i,W}}\right)^{-1}$	1.25
Windows	$U_{W_{\text{win}}} = \left(\sum_{i=1}^{p} \frac{1}{\lambda_{i,W_{\text{win}}} \cdot d_{i,W_{\text{win}}}}\right)^{-1}$	3.25
Floors	$U_F = \left(\sum_{i=1}^{m} \frac{1}{\lambda_{i,F} \cdot d_{i,F}}\right)^{-1}$	0.80
Ceilings	$U_C = \left(\sum_{i=1}^{m} \frac{1}{\lambda_{i,C} \cdot d_{i,C}}\right)^{-1}$	0.90
Doors	$U_D = \left(\sum_{i=1}^{m} \frac{1}{\lambda_{i,D} \cdot d_{i,D}}\right)^{-1}$	2.50

Table 1. Building physics features and U-values for simulations, where $\lambda_{i,j}$ represents the thermal conductivity and $d_{i,j}$ the thickness of the i-th layer.

Using CFD and thermal modelling, this study analyzes heat transfer dynamics within the TBIM environment, considering convection, conduction and radiation to predict temperature distributions in real-world environments.
Simulations have been conducted on *Zone A*, with data from devices serving as ground truth for model calibration, forming the basis for heat transfer and diffusion simulations.

3.4.2 Boundary conditions

Climate data from the Climate.OneBuilding database is integrated into the model, with geographic coordinates extracted via the Geopy library[4] to calculate annual temperature extremes. The system processes hourly weather data to compute daily average temperatures for each month. The pre-processing pipeline includes:

- *Data cleaning:* removal of invalid entries such as missing or non-numeric values.
- *Outlier filtering:* Exclusion of extreme values to prevent anomalies in thermal simulations.

The cleaned dataset is then grouped by day and hour for each month. The formula for calculating the average temperature at each hour h of a day d is as follows (Equation 1):

$$T_{\text{avg}}(d,h) = \frac{1}{N}\sum_{i=1}^{N} T_i(d,h) \qquad \text{(Eq. 1)}$$

[4] https://geopy.readthedocs.io/en/stable/

Where:

- $T_{\text{avg}}(d,h)$is the average temperature for day d and hour h.
- N is the total number of records for that specific day and hour.
- $\sum_{i=1}^{N} T_i(d,h)$ is the sum of all temperature records for hour h on day d.

3.5 Computational Fluid Dynamics

The in-house code uses finite element-based computational fluid dynamics (CFD) in FEniCS platform to simulate heat transfer and airflow in an enclosed space under real-world environmental conditions. As illustrated in Figure 3, *Zone A* is divided into two sub-areas: *Zone A1* and *Zone A2*. Simulations were performed in both zones, with results averaged to ensure consistency with real-time data. The specific characteristics of these areas are detailed in Table 2.

Zone	Volume [m^3]	Radiators	Windows
Zone A1	208.65	3	4
Zone A2	56.04	1	1

Table 2. Characteristics of the two areas used in the simulation.

The geometric meshes of the converted model for simulations are enriched with U-values and IDLs information properties. The simulation integrates hourly outdoor temperatures with daily averages and incorporates predefined schedules for occupancy (Equation 2) and radiator heating.

$$occupancy\_schedule(h) = \begin{cases} 0, if\ h \in [19,24) \cup [0,8) \\ 1, if\ h \in [8,10) \\ 2, if\ h \in [10,12) \\ 0, if\ h \in [12,14) \\ 2, if\ h \in [14,19) \\ 0, otherwise \end{cases} \qquad \text{(Eq. 2)}$$

The Navier-Stokes equations for modelling heat transfer within the room are numerically solved using the finite element method (FEM). These equations for incompressible fluid flow are calculated over a structured 3D mesh volume representing the room (Section 3.3).
In this case, using FEniCS library, equations are transformed into weak forms for efficient numerical approximation. This involves multiplying the governing equations by a test function and integrating over the computational domain (Ω).
Below, the weak forms used for momentum conservation (Navier-Stokes, Equation 3), continuity (incompressibility, Equation 4), and heat transfer (Equation 5) are given (Stokes, 1851):

$$\frac{\partial \boldsymbol{u}}{\partial t} + (\boldsymbol{u}\cdot\nabla)\boldsymbol{u} - \nu\nabla^2\boldsymbol{u} + \nabla p = \boldsymbol{F} \qquad \text{(Eq. 3)}$$

$$\int_\Omega \left(\frac{\partial \boldsymbol{u}}{\partial t} + (\boldsymbol{u}\cdot\nabla)\boldsymbol{u} - \nu\nabla^2\boldsymbol{u} + \nabla p - \boldsymbol{F}\right)\cdot \boldsymbol{v}\, d\Omega = 0 \qquad \text{(Eq. 4)}$$

$$\frac{\partial T}{\partial t} + \boldsymbol{u}\cdot\nabla T - \alpha\nabla^2 T = S \qquad \text{(Eq. 5)}$$

Where:

- $\boldsymbol{u}$ is the velocity vector field;
- t is time [s, min, h];
- $\frac{\partial \boldsymbol{u}}{\partial t}$ transient term, that is the fluid acceleration;
- $(\boldsymbol{u}\cdot\nabla)\boldsymbol{u}$ is the convective term, the fluid inertia;
- $\nu\nabla^2\boldsymbol{u}$ is the diffusion term, so the viscous effect;
- ∇p is the gradient of pressure;

- $\boldsymbol{F}$, the external forces, when present.

This formulation ensures a physically consistent simulation of heat transfer and fluid dynamics within the room of *Zone A*, allowing for accurate thermal and flow behaviour predictions.
The space is discretized into volumetric elements of *vs* = 0.25m ×0.25m ×0.25 m to enhance accuracy and stability.
Indoor temperature dynamics are influenced by thermal boundary conditions and occupant-generated heat (80 W/person), which is incorporated into the model and varies throughout the day.
By integrating thermal boundary conditions and external climate data, this simulation provides a detailed representation of indoor temperature distribution and energy efficiency.

3.6 Wall masks extraction

Wall masks to identify available areas for sensor installation are generated starting from 3D classified information then projected onto 2D planes (Figure 7 – left). We start by isolating the wall class from the classified point data and the floors to delimit walls dimension.
Once walls and floors are separated, we utilize the graph that connects the classified point cloud and geometries as a reference.
In particular, using the wall structure as a reference, we extract its starting $p_{\text{start}} = (x_{\text{start}}, y_{\text{start}}, z_{\text{start}})$ and ending point $p_{\text{end}} = (x_{\text{end}}, y_{\text{end}}, z_{\text{end}})$. With these points, we compute the main axis of the wall (Equation 6) in the *xy* plane, and we determine its direction, as described in (Equation 7).

$$\boldsymbol{v}_{wl} = (x_{\text{end}} - x_{\text{start}}, y_{\text{end}} - y_{\text{start}}, z_{\text{end}} - z_{\text{start}}) \quad \text{(Eq. 6)}$$

$$v_{mi} = \frac{v_{wl}}{|v_{wl}|} \quad \text{(Eq. 7)}$$

Where $|\boldsymbol{v}_{\text{wl}}| = \sqrt{(x_{\text{end}} - x_{\text{start}})^2 + (y_{\text{end}} - y_{\text{start}})^2 + (z_{\text{end}} - z_{\text{start}})^2}$.

Then, we compute the offset axis, which is positioned 1 meter away from the main axis, in the middle area of the wall, and we set the *z*-coordinate to the mean height of the wall.
Finally, we can automatically fix the camera position for each wall (Equation 8):

$$P_{\text{camera}} = (x_{\text{mean}} + 1, y_{\text{mean}} + 1, z_{\text{mean}}) \quad \text{(Eq. 8)}$$

Where:

- $x_{\text{mean}} = \frac{x_{\text{start}} + x_{\text{end}}}{2}$,
- $y_{\text{mean}} = \frac{y_{\text{start}} + y_{\text{end}}}{2}$,
- $z_{\text{mean}} = \frac{z_{\text{start}} + z_{\text{end}}}{2}$.

Once these computations are completed, we generate ortho images of the classified point cloud (Figure 7).
After obtaining the ortho images of the indoor walls, we apply the Canny edge detection algorithm (Canny, 1986) to identify the edges within these images. To refine the extracted masks, we finally apply the DBSCAN (Ester et al., 1996) algorithm to create masks that highlight areas of the image suitable for sensor installation. In particular, Figure 7 illustrates sensor placement suitability: coloured pixels on the left and white pixels on the right indicate available areas, while white pixels on the left and black pixels on the right represent areas not suitable for sensor installation.
This multi-step process effectively identifies the most suitable regions of the point cloud for sensor placement, considering the geometric properties of the walls, indoor clutter, and spatial relationships within the environment.

4. Results and simulations

This section presents the simulation results for *Zone A* indoor spaces, incorporating key boundary conditions such as outdoor temperatures, occupancy levels, radiator parameters, and real-time temperature data from IoT devices. The analysis focuses on the TBIM model, derived from the gDT, with an emphasis on energy simulations and CFD analysis.

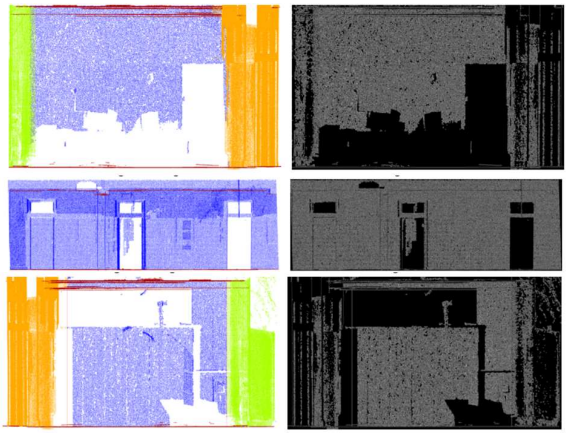

Figure 7. Wall masks indicating available areas (colored on the left, white on the right) or unavailable areas (white on the left, black on the right) for sensor placement.

4.1 The model for the simulations

The gDT model reconstructs the building's structural elements using meshes. In the FEniCS library, a mesh represents the computational domain where finite element methods (FEM) are applied. It consists of discrete elements, commonly tetrahedra in 3D, that partition the domain for numerical analysis (Figure 8).
As outlined in Section 3.4.1, and reported in Figure 1, the mesh preparation workflow includes importing the .obj file into Blender (*v. 4.3*), exporting it as .stl for compatibility with meshing tools, and converting the .stl file to .xdmf format in FEniCS for simulations.

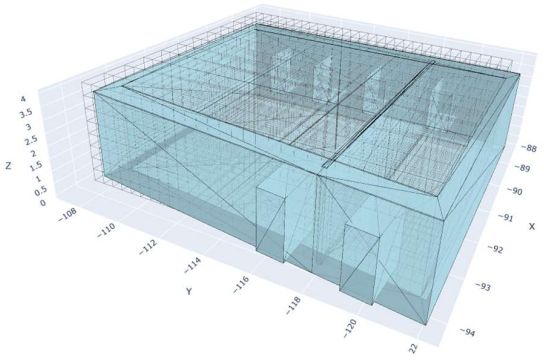

Figure 8. Indoor volume with discretized volumes.

This structured approach ensures that the computational domain is properly discretized and optimized for FEM-based heat transfer. Figure 8 illustrates the discretized volume used for the analysis, generated with *UnitCubeMesh(vs, vs, vs)*, where *vs* represents the dimension of the discretized volume. For visualization purposes, *vs* is set to 0.50 m, while for simulation, a finer resolution of *vs* = 0.25 m is used.

4.2 Model calibration

The calibration process begins with the collection of thermal data from IoT sensors placed throughout the building, capturing temperature readings every minute. This data is combined with outdoor temperature values from the .epw file, which provides essential external climate information. By using this combined dataset, multiple CFD simulations are performed to replicate the building’s thermal behavior, focusing particularly on the performance of the radiators. The main parameter assessed is the radiator efficiency (η), which reflects how effectively the radiators heat the space in relation to their energy consumption. The simulation results are compared to the real-world data from the IoT devices, allowing for iterative adjustments of the model. Simulations indicate that indoor temperatures tend to be slightly higher than the recorded values, likely caused by internal heat buildup, material thermal variations, or occupancy patterns. Furthermore, the evening temperature drop suggests the model may slightly underestimate heat loss.
Figure 9 illustrates temperature variations for the *Zone A2*, the smaller one, for a day in early March, where the temperatures are more evenly distributed with minimal fluctuations throughout the day. This fine-tuning process is crucial to ensure that the CFD model accurately represents the building's heating dynamics, leading to more reliable predictions of indoor thermal conditions.

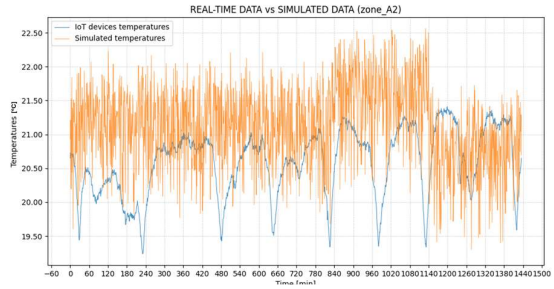

Figure 9. Comparison between real-time data (blue graph) and simulated data (orange graph).

4.3 Results for CFD simulations

For a comprehensive analysis of indoor spaces, simulations were conducted across the entire *Zone A*.
These simulations were performed for specific days within the available monthly data, as well as on a monthly basis. This approach enables model calibration using both daily temperature data and monthly ground truth data.
The in-house code simulations were conducted on a system equipped with a NVIDIA® GeForce RTX™ 4050 GPU with 6GB GDDR6 memory, ensuring high computational performance and efficiency. Simulations took around 10 hours to be computed.
The mean error calculated between the real-time temperature data and the simulated one is (Equation 9):

$$\bar{E} = \frac{1}{n}\sum_{i=1}^{n}\left|t_{\mathrm{IoT},i} - t_{\mathrm{simul},i}\right| \qquad \text{(Eq. 9)}$$

Where $t_{\mathrm{IoT},i}$ is the temperature recorded by IoT device at time i, $t_{\mathrm{simul},i}$ is the temperature simulated at time i, n is the number of data points (e. g., $n = 1440$ for a daily simulation). This value is $\bar{E} = 0.644$ °C for daily and $\bar{E} = 1.67$ °C for monthly simulation.
Figure 10 shows the average distribution of heat during the day as a point cloud distribution of temperature for better visualization. Furthermore, as explained before, the internal volume has been discretized in smaller volumes (vs = 0.25m) where it is possible to evaluate the changing temperature during the day in different parts of the indoor environment. This structure enables the visualization of the average daily temperature distribution near indoor walls.

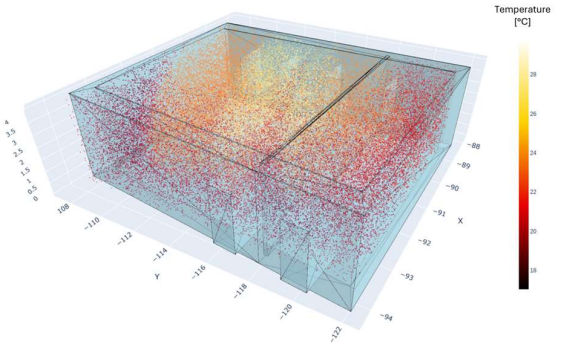

Figure 10. CFD simulation of heat distribution in Zone A.

Figure 11 shows two different timesteps of two of the discretized volumes, at t_1 = 720 minutes and t_2 = 1200 minutes, located near walls close to the windows.
Figures 11a and 11b illustrate the positioning of these sample volumes (defined as *Volume_01, Volume_02*) within *Zone A*, while Figures 11c to 11f show the heat distribution at two different time points, t_1 and t_2.

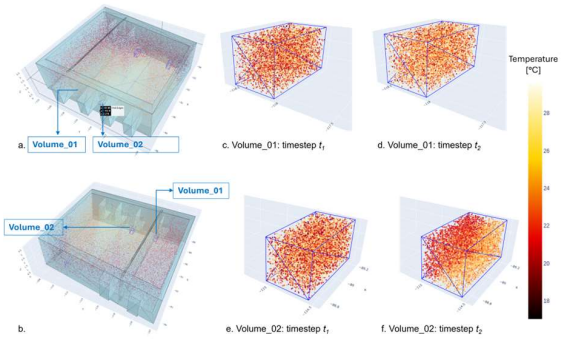

Figure 11. Heat distribution in two sampled volumes.

Following Section 3.6, orthogonal wall images, points, and temperature values are extracted, with each point defined by coordinates and the simulated temperature (p_{temp}).
Using the same workflow, a 1-meter influence area around each wall is established, divided into four discretized volumes.
The main plane of the wall (Equation 10) is computed based on its normal vector, derived from (Equation 11), ensuring accurate spatial alignment of the extracted temperature data.

$$n_x(x - x_{start}) + n_y(y - y_{start}) + n_z(z - z_{start}) = 0 \qquad \text{(Eq. 10)}$$

$$n_{\mathrm{w}} = (n_x, n_y, n_z) \qquad \text{(Eq. 11)}$$

Where $(x_{start}, y_{start}, z_{start})$ is a specific point on the plane and (x, y, z) is any arbitrary point on the plane, while $n_{\mathrm{w}} = (n_x, n_y, n_z)$ represents the components of the normal vector.
Then, we collect the points close to the wall plane if the distance of a point is less than 1 m ($d_{\mathrm{wall}} < 1{,}00\ m$), where d_{wall} is defined in Equation 12. Finally, we project these points into the main plane, maintaining color visualization.
This method ensures the acquisition of orthoimages of walls, which can then be compared to wall masks.

$$d_{\text{wall}} = \frac{|n_x(x_p - x_{\text{start}}) + n_y(y_p - y_{\text{start}}) + n_z(z_p - z_{\text{start}})|}{\sqrt{n_x^2 + n_y^2 + n_z^2}} \quad \text{(Eq. 12)}$$

By analysing these zones, it is possible to identify areas where the heat gradient is lower, helping to determine the optimal placement for sensors.

4.4 Sensor placement

The final step serves to detect thermal stagnation regions in images, where temperature remains stable across various scenarios. These zones are ideal for sensor placement, ensuring consistent and accurate thermal monitoring with minimal influence from external factors.

The output masks from Section 3.6 highlight available pixels indicating suitable sensor locations (Figure 7) and serve as the foundation for defining areas where sensors can be placed.

Simulations conducted on daily-based data provide (i) average temperatures for each day, calculated from hourly data, and (ii) average temperatures for the month, derived from daily.

Figure 12 illustrates the pipeline used to integrate these two outputs, identifying the most suitable areas for sensor placement. Specifically, the CFD simulation utilizes these temperature values to generate an hourly heat distribution, which is then converted into a point cloud representing the heat distribution (Figure 12a). The process then follows these steps:

1. ***Point collection near the walls:*** following the procedure outlined in Section 4.3, we collect points corresponding to each wall within a distance of $d_{\text{wall}} < 1\,m$ (Figure 12b).
2. ***Projection and orthoimage plotting:*** these points are projected and orthoimages of the walls are created, displaying the points and their associated temperatures (p_{temp}) (Figures 12c, 12d).
3. ***Time-based heat distribution visualization:*** by plotting these for each hour, starting from time $t = 0$ with initial conditions and continuing with t_i and then $t_{(i+1)}$, we visualize the heat distribution near each wall (Figure 12e).
4. ***Determining sensor placement:*** by combining the CFD temperature simulations, which highlight areas with stagnant heat, and the masks indicating sensor placement availability, we determine the most suitable sensor locations (Figure 12f).

This approach enables the strategic placement of sensors in thermal stagnation zones, improving thermal comfort assessment and optimizing overall climate control efficiency.

5. Conclusions

The proposed workflow optimizes sensor placement through a semi-automated pipeline, converting point cloud data into a 3D model suitable for CFD simulations.

These simulations analyze indoor heat diffusion, identifying stable thermal zones with minimal heat fluctuation to optimize heating and cooling system sizing for improved efficiency.

By adapting to real-world conditions, the proposed approach enhances BEMS by refining thermal regulation, reducing energy consumption, and enabling precise real-time control to enhance overall building performance.

This pipeline revealed challenges in both workflow components, i.e. (i) the geometric modeling and (ii) the simulation. Specifically, the automatically derived TBIM model introduces mesh complexities that hinder compatibility with industry-specific CFD software like OpenFOAM. To ensure accurate shape interpretation, future work will refine parameters for improved integration and accuracy.

On the other hand, simulations tend to slightly overestimate indoor temperatures compared to measured values, likely due to internal heat accumulation, variations in thermal properties, or occupancy patterns. Additionally, the observed temperature drop at the end of the day suggests that the simulated building envelope may underestimate heat loss dynamics.

Conversely, the FEniCS library has demonstrated high flexibility and efficiency in managing both geometries and heat transfer analysis, making it a valuable tool for further improvements.

Future work will focus on evaluating the effects of gDT quality and topological accuracy on sensor placement uncertainty, aiming to quantify how variations in geometric and topological representations influence the reliability and precision of sensor positioning within the built environment. Additionally, as more data becomes available, further improvements will be made to enhance simulation precision, better capturing real-world thermal dynamics and refining model validation.

Acknowledgements

This research is partially supported by the EU InCUBE project (https://incubeproject.eu), funded by the European Union under Grant Agreement No. 101069610. We extend our gratitude to Tera Srl for providing IoT devices and related data, and to Comune di Trento for its collaboration in installing these devices. We also thank Centro Servizi Culturali Santa Chiara for granting access to their spaces for this study. Finally, we acknowledge the support of Edilvi S.p.A. and the University of Trento for their contribution to the co-financed program funded by the European Union - Next Generation EU, Mission 4 Component 2 CUPE66E22000050008.

References

Aish, R., Jabi, W., Lannon, S., Wardhana, N.M., Chatzivasileiadi, A., 2018. Topologic: Tools to explore architectural topology. *AAG*, 316-341.

Arowoiya, V. A., Moehler, R. C., Fang, Y., 2024. Digital twin technology for thermal comfort and energy efficiency in buildings: A state-of-the-art and future directions. *Energy and Built Environment, 5*(5), 641-656.

Bassier, M., Vermandere, J., De Geyter, S., De Winter, H., 2024. GEOMAPI: Processing close-range sensing data of construction scenes with semantic web technologies. *Automation in construction, 164,* 105454.

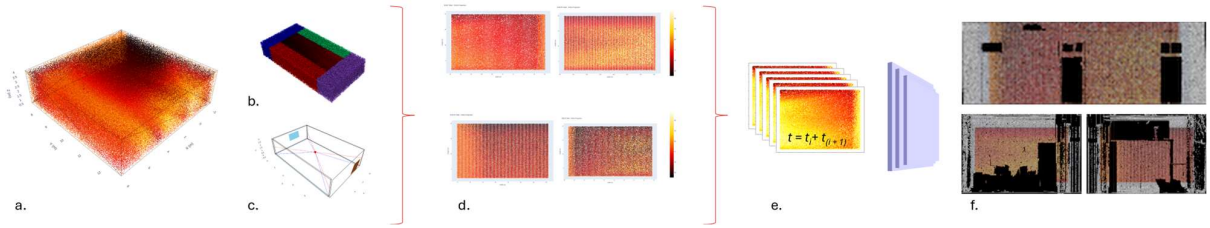

Figure 12. Pipeline to extract the most suitable position for sensors placement.

Blut, C., Becker, R., Kinnen, T., Schluetter, D., Emunds, C., Frisch, J., Heidermann, D., Wenthe, M., Rettig, T., Baranski, M., van Treeck, C., Blankenbach, J., 2024. Optimizing Building Energy Systems through BIM-enabled georeferenced Digital Twins. *ISPRS Archives, XLVIII-4/W11-2024*, 1–2024.

Canny, J., 1986. A computational approach to edge detection. *IEEE TPAMI-8(6),* pp. 679-698.

Ester, M., Kriegel, H.-P., Sander, J., Xu, X., 1996. A density-based algorithm for discovering clusters in large spatial databases with noise. *Proc. of the 2nd Intern. Conference on Knowledge Discovery and Data Mining (KDD)*, pp. 226-231.

Gosavi, A., Le, V.K., 2024. Maintenance optimization in a digital twin for Industry 4.0. *Ann. Oper. Res. 340,* 245–269.

Hu, K., Han, D., Qin, G., Zhou, Y., Chen, L., Ying, C., Guo, T., Liu, Y., 2023. Semi-automated Generation of Geometric Digital Twin for Bridge Based on Terrestrial Laser Scanning Data. *Advances in Civil Engineering*, 1–13.

Jabi, W., Chatzivasileiadi, A., 2021. Topologic: Exploring spatial reasoning through geometry, topology, and semantics. *Formal methods in architecture*, 277-285.

Lin, D., Jarzabek-Rychard, M., Tong, X., Maas, H.-G., 2019. Fusion of thermal imagery with point clouds for building façade thermal attribute mapping. *ISPRS Journal of Photogrammetry and Remote Sensing*, *151*, 162-175.

Liu, S., Zeng, Z., Ren, T., Li, F., Zhang, H., Yang, J., Li, C., Yang, J., Su, H., Zhu, J., Zhang, L., 2023. Grounding dino: Marrying dino with grounded pre-training for open-set object detection. *arXiv preprint arXiv:2303.05499.*

Liu, S., Zheng, P., Bao, J., 2024a. Digital Twin-based manufacturing system: a survey based on a novel reference model. *J. Intell. Manuf. 35,* 2517–2546.

Liu, Z., Lang, Z.-Q., Gui, Y., Zhu, Y.-P., & Laalej, H., 2024b. Digital twin-based anomaly detection for real-time tool condition monitoring in machining. *Journal of Manufacturing Systems, 75*, 163-173.

Logg, A., Wells, G., Mardal, K.-A., 2011. Automated Solution of Differential Equations by the Finite Element Method: The FEniCS Book. *Lecture Notes in Computational Science and Engineering*, 84. Springer, Berlin, Heidelberg.

Ma, R., Li, Q., Zhang, B., Huang, H., Yang, C., 2024. An ontology-driven method for urban building energy modelling. *Sustainable Cities and Society*.

Maduta, C., D'Agostino, D., Tsemekidi-Tzeiranaki, S., Castellazzi, L., Melica, G., Bertoldi, P., 2023: Towards climate neutrality within the European Union: Assessment of the Energy Performance of Buildings Directive implementation in Member States. *Energy and Buildings*, 301, 113716.

Olasolo-Alonso, P., López-Ochoa, L. M., Las-Heras-Casas, J., López-González, L. M., 2023. Energy performance of buildings directive implementation in Southern European countries: A review. *Energy and Buildings, 281,* 112751.

OpenCFD Ltd., OpenFOAM: The Open Source CFD Toolbox, Available at: https://www.openfoam.org.

Pan, Y., Wang, M., Lu, L., Wei, R., Cavazzi, S., Peck, M., & Brilakis, I., 2024. Scan-to-graph: Automatic generation and representation of highway geometric digital twins from point cloud data. *Automation in Construction, 166*, 105654.

Ramón-Constantí, A., Adán-Oliver, A., Castilla-Pascual, F.J., Pérez-Andreu, V., 2024. An experimental methodology for the calibration of indoor building environment models using thermal point clouds and CFD simulation. *Advances in Building Energy Research*, *18(3)*, 261–294.

Roman, O., Farella, E. M., Rigon, S., Remondino, F., Ricciuti, S., Viesi, D., 2023. From 3D surveying data to BIM to BEM: the InCUBE dataset. *ISPRS Arch. Photogramm., Remote Sens. and Spatial Inf. Sci.,* XLVIII-1/W3-2023, 175–182.

Roman, O., Mazzacca, G., Farella, E. M., Remondino, F., Bassier, M., Agugiaro, G., 2024a. Towards Automated BIM and BEM Model generation using a B-Rep-based Method with Topological Map. *ISPRS Annals of the Photogramm., Remote Sens. and Spatial Inf. Sci., X-4-2024,* 287–294.

Roman, O., Bassier, M., De Geyter, S., De Winter, H., Farella, E. M., and Remondino, F., 2024b. BIM Module for Deep Learning-driven parametric IFC reconstruction. *ISPRS Arch. Photogramm. Remote Sens. Spatial Inf. Sci., XLVIII-2/W8-2024*, 403–410.

Stokes, G.G., 1851. On the effect of the internal friction of fluids on the motion of pendulums. *Trans. Camb. Philos. Soc., 8,* 287–305.

Wandel, N., Weinmann, M., Klein, R., 2020. Fast Fluid Simulations in 3D with Physics-Informed Deep Learning. *arXiv preprint arXiv:2012.11893*.

Wu, X., Jiang, L., Wang, P.-S., Liu, Z., Liu, X., Qiao, Y., Ouyang, W., He, T., Zhao, H., 2024. Point Transformer V3: Simpler, Faster, Stronger. *arXiv preprint*, arXiv:2312.10035.

Yang, Z., Gaidhane, A. D., Drgoňa, J., Chandan, V., Halappanavar, M. M., Liu, F., Cao, Y., 2024. Physics-constrained graph modeling for building thermal dynamics. *Energy and AI, 16*, 100346.

Yue, Y., Kontogianni, T., Schindler, K., Engelmann, F., 2023. Connecting the Dots: Floorplan Reconstruction Using Two-Level Queries. *Proc. CVPR*.

Zhao, H., Jiang, L., Jia, J., Torr, P., Koltun, V., 2021. Point Transformer. *Proc. ICCV,* 16259–16268.

Ziozas, N., Kitsopoulou, A., Bellos, E., Iliadis, P., Gonidaki, D., Angelakoglou, K., Nikolopoulos, N., Ricciuti, S. and Viesi, D., 2024. Energy Performance Analysis of the Renovation Process in an Italian Cultural Heritage Building. *Sustainability*, *16*(7), p. 2784.